Bull. Korean Math. Soc. **55** (2018), No. 3, pp. 881–898
https://doi.org/10.4134/BKMS.b170357
pISSN: 1015-8634 / eISSN: 2234-3016

AN IMPLICIT NUMERICAL SCHEME FOR SOLUTION OF INCOMPRESSIBLE NAVIER-STOKES EQUATIONS ON CURVILINEAR GRIDS

Hassan Fayyaz and Abdullah Shah

Abstract. This article deals with implementation of a high-order finite difference scheme for numerical solution of the incompressible Navier-Stokes equations on curvilinear grids. The numerical scheme is based on pseudo-compressibility approach. A fifth-order upwind compact scheme is used to approximate the inviscid fluxes while the discretization of metric and viscous terms is accomplished using sixth-order central compact scheme. An implicit Euler method is used for discretization of the pseudo-time derivative to obtain the steady-state solution. The resulting block tridiagonal matrix system is solved by approximate factorization based alternating direction implicit scheme (AF-ADI) which consists of an alternate sweep in each direction for every pseudo-time step. The convergence and efficiency of the method are evaluated by solving some 2D benchmark problems. Finally, computed results are compared with numerical results in the literature and a good agreement is observed.

1. Introduction

The incompressible Navier-Stokes equations are fundamental equations in fluid mechanics. The numerical study of these equations is very important due to its various applications. Numerous computational methods have been developed and are still one of the central aspects of the research area known as computational fluid dynamics (CFD). Increasing interest in high-performance computing for problems acquiring high accuracy for a wide range of length scales, such as large-eddy simulation and direct numerical simulation of turbulence, high-order numerical methods become a major concern. The main objective of this work is to develop a high-order finite difference scheme in generalized curvilinear coordinates capable of treating a wider spectrum of problems with non-uniform grids. In 2D Cartesian coordinates system with (u, v) as the velocity field and p as the pressure, the non-dimensional form of

Received April 18, 2017; Revised January 29, 2018; Accepted February 1, 2018.
2010 *Mathematics Subject Classification.* 65N06, 76D05, 65D25.
Key words and phrases. incompressible Navier-Stokes equations, curvilinear coordinate, artificial compressibility method, alternate direction implicit method.

incompressible Navier-Stokes equations are:

$$\frac{\partial u}{\partial x}+\frac{\partial v}{\partial y}=0, \tag{1}$$

$$\frac{\partial u}{\partial t}+u\frac{\partial u}{\partial x}+v\frac{\partial u}{\partial y}=-\frac{\partial p}{\partial x}+\frac{1}{\mathrm{Re}}\left(\frac{\partial^2 u}{\partial x^2}+\frac{\partial^2 u}{\partial y^2}\right), \tag{2}$$

$$\frac{\partial v}{\partial t}+u\frac{\partial v}{\partial x}+v\frac{\partial v}{\partial y}=-\frac{\partial p}{\partial y}+\frac{1}{\mathrm{Re}}\left(\frac{\partial^2 v}{\partial x^2}+\frac{\partial^2 v}{\partial y^2}\right). \tag{3}$$

Here Re is Reynolds number and defined as $\mathrm{Re}=\frac{\rho v_\infty L}{\mu}$ with v_∞ being the reference velocity, L the characteristic length, ρ the density and μ the dynamic viscosity of the fluid. The continuity equation (1) lacks the pressure term which makes it difficult to solve it implicitly. However, in the compressible Navier-Stokes equations, the time dependent term in the mass conservation equation allows to solve for the density directly, this gives motivation to develop methods for incompressible flows based on compressible flow methods known as artificial compressibility (or pseudo-compressibility) method [3, 4]. In this method, the time derivative of pressure is added to the continuity equation that will not only provide solution for p but also on convergence (reaching steady state), it satisfies the mass conservation as well. The continuity equation is modified as;

$$\frac{\partial p}{\partial \tau}+\beta\left(\frac{\partial u}{\partial x}+\frac{\partial v}{\partial y}\right)=0, \tag{4}$$

where τ is pseudo-time or iteration parameter and β is the artificial compressibility factor. The main advantage of this method is to use compressible flow solver for numerical solution of incompressible flow. This method has a drawback that the artificial compressibility factor β may affect the convergence rate of computation. It is difficult to give optimal value of this factor in advance. However it can be found by numerical experiments on coarse grids before going to solution on finer grids as shown in Figure 2(a).

2. Mathematical formulation and discretization schemes

2.1. Governing equations

The governing equations are transformed in generalized curvilinear coordinates (ξ,η) using artificial compressibility term in conservative form and by replacing t with τ in equations (2), (3) (see [19] and references therein)

$$\frac{\partial \hat{\mathbf{D}}}{\partial \tau}+\frac{\partial(\hat{\mathbf{G}}-\hat{\mathbf{G}}_v)}{\partial \xi}+\frac{\partial(\hat{\mathbf{H}}-\hat{\mathbf{H}}_v)}{\partial \eta}=0, \tag{5}$$

where $\hat{\mathbf{D}}=\frac{\mathbf{D}}{J}=\frac{1}{J}\begin{pmatrix}p\\u\\v\end{pmatrix}$ is solution vector, J being Jacobian of transformation. $\hat{\mathbf{G}}$ and $\hat{\mathbf{H}}$ are inviscid flux vectors while $\hat{\mathbf{G}}_v$ and $\hat{\mathbf{H}}_v$ viscous flux vectors and

are given

$$\hat{\mathbf{G}} = \frac{1}{J}\begin{pmatrix} \beta U \\ uU + \xi_x p \\ vU + \xi_y p \end{pmatrix},\ \hat{\mathbf{H}} = \frac{1}{J}\begin{pmatrix} \beta V \\ uV + \eta_x p \\ vV + \eta_y p \end{pmatrix},$$

$$\hat{\mathbf{G}}_v = \frac{1}{\mathrm{Re}J}\begin{bmatrix} 0 \\ \left(\xi_x^2 + \xi_y^2\right) u_\xi + \left(\xi_x\eta_x + \xi_y\eta_y\right) u_\eta \\ \left(\xi_x^2 + \xi_y^2\right) v_\xi + \left(\xi_x\eta_x + \xi_y\eta_y\right) v_\eta \end{bmatrix},$$

$$\hat{\mathbf{H}}_v = \frac{1}{\mathrm{Re}J}\begin{bmatrix} 0 \\ \left(\xi_x\eta_x + \xi_y\eta_y\right) u_\xi + \left(\eta_x^2 + \eta_y^2\right) u_\eta \\ \left(\xi_x\eta_x + \xi_y\eta_y\right) v_\xi + \left(\eta_x^2 + \eta_y^2\right) v_\eta \end{bmatrix}.$$

The contravariant velocity vectors are U and V in their respective curvilinear directions, and are given as

$$U = \xi_x u + \xi_y v,$$
$$V = \eta_x u + \eta_y v.$$

The terms involving the geometry of the grids, such as ξ_x, ξ_y, η_x, η_y are called metrics. The inviscid flux vector in any direction can be uniformly written as

$$\hat{k}_x\mathbf{G} + \hat{k}_y\mathbf{H} = \hat{\mathbf{G}}_k$$

$$\hat{k}_x\begin{pmatrix} \beta u \\ u^2 + p \\ vu \end{pmatrix} + \hat{k}_y\begin{pmatrix} \beta v \\ uv \\ v^2 + p \end{pmatrix} = \begin{pmatrix} \beta\alpha \\ u\alpha + \hat{k}_x p \\ v\alpha + \hat{k}_y p \end{pmatrix}, \tag{6}$$

where $\alpha = \hat{k}_x u + \hat{k}_y v$, $(\hat{k}_x, \hat{k}_y) = (k_x, k_y)/J$, $k = \xi, \eta$.

The Jacobian matrix of the inviscid flux vector is:

$$\hat{\mathbf{A}}_k = \frac{\partial\hat{\mathbf{G}}_k}{\partial\mathbf{D}} = \begin{pmatrix} 0 & \hat{k}_x\beta & \hat{k}_y\beta \\ \hat{k}_x & \hat{k}_x u + \alpha & \hat{k}_y u \\ \hat{k}_y & \hat{k}_x v & \hat{k}_y v + \alpha \end{pmatrix}, \tag{7}$$

which can be diagonalized as

$$\hat{\mathbf{A}}_k = \mathbf{T}_k\Lambda_k\mathbf{T}_k^{-1}, \tag{8}$$

with eigenvalue matrix $\Lambda_k = \mathrm{diag}(\lambda + \varrho, \lambda, \lambda - \varrho)$, where ϱ is the pseudo-speed of sound given by

$$\varrho = \sqrt{\lambda^2 + \beta(\hat{k}_x^2 + \hat{k}_y^2)}.$$

The right and left eigenvector matrices are $\mathbf{T}_k$ and $\mathbf{T}_k^{-1}$ respectively. The hyperbolic nature of the artificial compressibility formulation provides basis for the development of upwind schemes.

2.2. Discretization of convective terms

The convective terms in the incompressible Navier-Stokes equations are first split in the positive and negative flux depending upon the sign of eigenvalues of the flux Jacobian. For example in ξ direction,

$$\hat{\mathbf{G}}_\xi = \hat{\mathbf{G}}_\xi^+ + \hat{\mathbf{G}}_\xi^-, \tag{9}$$

where $\hat{\mathbf{G}}_\xi^+$ corresponds to the information being propagated by the positive eigenvalues in the positive direction where as $\hat{\mathbf{G}}_\xi^-$ corresponds to the information being propagated by the negative eigenvalues in the negative direction. To evaluate the values of the derivatives in Eq. (9), the following fifth-order upwind compact scheme [7,8] at interior points is used:

$$\text{at } i = 3:$$

$$\frac{3}{5}[\hat{\mathbf{G}}_\xi^+]_i + \frac{2}{5}[\hat{\mathbf{G}}_\xi^+]_{i-1} = \frac{-\Delta^-\hat{\mathbf{G}}_{i+2}^+ + 11\Delta^-\hat{\mathbf{G}}_{i+1}^+ + 47\Delta^-\hat{\mathbf{G}}_i^+ + 3\Delta^-\hat{\mathbf{G}}_{i-1}^+}{60\Delta\xi}, \tag{10a}$$

$$\text{at } i = N-2:$$

$$\frac{3}{5}[\hat{\mathbf{G}}_\xi^-]_i + \frac{2}{5}[\hat{\mathbf{G}}_x^-]_{i+1} = \frac{-\Delta^+\hat{\mathbf{G}}_{i-2}^- + 11\Delta^+\hat{\mathbf{G}}_{i-1}^- + 47\Delta^+\hat{\mathbf{G}}_i^- + 3\Delta^+\hat{\mathbf{G}}_{i+1}^-}{60\Delta\xi}, \tag{10b}$$

respectively, where $\Delta^-\hat{\mathbf{G}}_i = \hat{\mathbf{G}}_i - \hat{\mathbf{G}}_{i-1}$ and $\Delta^+\hat{\mathbf{G}}_i = \hat{\mathbf{G}}_{i+1} - \hat{\mathbf{G}}_i$.

The difference of grid is $\Delta\xi$ in the computational space. From equation (6), the difference in flux between two neighboring points in ξ direction is

$$\begin{aligned}
\hat{\mathbf{G}}_{i+1} - \hat{\mathbf{G}}_i &= \left(\hat{\xi}_x\mathbf{G} + \hat{\xi}_y\mathbf{H}\right)_{i+1} - \left(\hat{\xi}_x\mathbf{G} + \hat{\xi}_y\mathbf{H}\right)_i \\
&= \left(\overline{\xi}_x \triangle \mathbf{G} + \overline{\xi}_y \triangle \mathbf{H}\right) + \overline{\mathbf{G}} \triangle \hat{\xi}_x + \overline{\mathbf{H}} \triangle \hat{\xi}_y \\
&= \left(\overline{\xi}_x\mathbf{A}_\xi(\overline{\mathbf{D}}) \triangle \mathbf{D} + \overline{\xi}_y\mathbf{A}_\eta(\overline{\mathbf{D}}) \triangle \mathbf{D}\right)_i + \overline{\mathbf{G}} \triangle \hat{\xi}_x + \overline{\mathbf{H}} \triangle \hat{\xi}_y \\
&= A^\pm_{i+\frac{1}{2}}(\overline{\mathbf{D}}) \triangle \mathbf{D} + \overline{\mathbf{G}} \triangle \hat{\xi}_x + \overline{\mathbf{H}} \triangle \hat{\xi}_y,
\end{aligned} \tag{11}$$

where $\overline{\mathbf{G}}$ and $\overline{\mathbf{H}}$ be the arithmetic average of inviscid fluxes in cartesian coordinates $\mathbf{G}$ and $\mathbf{H}$ respectively between points i and $i+1$, $\triangle$ be the difference between points i and $i+1$. The remaining two terms in first line of equation (11) shows the influence of varying grids. The Jacobian matrix in split form is given by $\hat{\mathbf{A}}^\pm_{i+\frac{1}{2}}(\overline{D}) = \mathbf{T}_A\Lambda_A^\pm\mathbf{T}_A^{-1}$, with $\Lambda_A^\pm = \frac{1}{2}(\Lambda_A \pm |\Lambda_A|)$, which is evaluated using arithmetic means of the flow variables as well as metrics between two consecutive grid points [17];

$$\overline{D} = \frac{1}{2}(D_i + D_{i+1}); (\overline{\xi}_x, \overline{\xi}_y) = \frac{1}{2}\left(\left(\hat{\xi}_x, \hat{\xi}_y\right)_i + \left(\hat{\xi}_x, \hat{\xi}_y\right)_{i+1}\right).$$

An explicit fourth-order one sided scheme [21] is used for the points next to boundary, i.e.,

$$\text{at } i = 2:$$

$$\left[\hat{\mathbf{G}}^{+}_{\xi}\right]_i = \frac{-3\hat{\mathbf{G}}^{+}_{i-1} - 10\hat{\mathbf{G}}^{+}_{i} + 18\hat{\mathbf{G}}^{+}_{i+1} - 6\hat{\mathbf{G}}^{+}_{i+2} + \hat{\mathbf{G}}^{+}_{i+3}}{12\Delta\xi}$$

$$= \frac{3\Delta\hat{\mathbf{G}}^{+}_{i-\frac{1}{2}} + 13\Delta\hat{\mathbf{G}}^{+}_{i+\frac{1}{2}} - 5\Delta\hat{\mathbf{G}}^{+}_{i+\frac{3}{2}} + \Delta\hat{\mathbf{G}}^{+}_{i+\frac{5}{2}}}{12\Delta\xi} \tag{12a}$$

at $i = N-1$:

$$\left[\hat{\mathbf{G}}^{-}_{\xi}\right]_i = \frac{3\hat{\mathbf{G}}^{-}_{i+1} + 10\hat{\mathbf{G}}^{-}_{i} - 18\hat{\mathbf{G}}^{-}_{i-1} + 6\hat{\mathbf{G}}^{-}_{i-2} - \hat{\mathbf{G}}^{-}_{i-3}}{12\Delta\xi}$$

$$= \frac{3\Delta\hat{\mathbf{G}}^{-}_{i+\frac{1}{2}} + 13\Delta\hat{\mathbf{G}}^{-}_{i-\frac{1}{2}} - 5\Delta\hat{\mathbf{G}}^{-}_{i-\frac{3}{2}} + \Delta\hat{\mathbf{G}}^{-}_{i-\frac{5}{2}}}{12\Delta\xi}. \tag{12b}$$

2.3. Discretization of metric and viscous terms

Computation of the Jacobian matrices require the calculations of first derivatives of x and y with respect to computational coordinates ξ and η. These first-order derivatives can be approximated with sixth-order central compact scheme [13];

$$\frac{1}{3}\psi'_{i-1} + \psi'_i + \frac{1}{3}\psi'_{i+1} = \frac{14}{9}\frac{\psi_{i+1} - \psi_{i-1}}{2\Delta\xi} + \frac{1}{9}\frac{\psi_{i+2} - \psi_{i-2}}{4\Delta\xi}, \tag{13}$$

which requires the solution of a tridiagonal system of equations. A fourth-order two sided compact scheme is used for the points near boundary, and a fourth-order upwind compact scheme [13] is used for the points on boundary respectively:

$$\text{at } i = 2 \text{ and } N-1: \ \frac{1}{4}\psi'_{i-1} + \psi'_i + \frac{1}{4}\psi'_{i+1} = \frac{3}{2}\frac{\psi_{i+1} - \psi_{i-1}}{2\Delta\xi}, \tag{14a}$$

$$\text{at } i = 1: \ 6\psi'_1 + 18\psi'_2 = \frac{-17\psi_1 + 9\psi_2 + 9\psi_3 - \psi_4}{\Delta\xi}, \tag{14b}$$

$$\text{at } i = N: \ 6\psi'_N + 18\psi'_{N-1} = \frac{17\psi_N - 9\psi_{N-1} - 9\psi_{N-2} + \psi_{N-3}}{\Delta\xi}. \tag{14c}$$

Since the discretization of second-order derivative has higher resolution than that of first-order derivatives. Therefore, central compact scheme for viscous terms is used. Also computation reduces to half if non-orthogonal grid is used for the second and mixed derivatives in viscous terms like $\partial_\xi\left(g\partial_\xi\psi\right)$ and $\partial_\xi\left(g\partial_\eta\psi\right)$. First, we expand second derivatives and mixed derivatives as follows

$$\partial_\xi\left(g\partial_\xi\psi\right) = \left(\partial_\xi g\right)\left(\partial_\xi\psi\right) + g\left(\partial_{\xi\xi}\psi\right), \tag{15a}$$

$$\partial_\xi\left(g\partial_\eta\psi\right) = \left(\partial_\xi g\right)\left(\partial_\eta\psi\right) + g\left(\partial_\xi\left(\partial_\eta\psi\right)\right), \tag{15b}$$

then compute all the first derivatives in the RHS of equation (15a) and equation (15b) using the fourth-order central compact scheme for metric terms as given in subsection (2.3). The second-order derivative $\partial_{\xi\xi}\psi$ is computed with

following sixth-order central compact scheme [13];

$$\begin{aligned} &2\psi''_{i-1} + 11\psi''_i + 2\psi''_{i+1} \\ &= 12\frac{\psi_{i-1} - 2\psi_i + \psi_{i+1}}{\Delta\xi^2} + \frac{3}{4}\frac{\psi_{i-2} - 2\psi_i + \psi_{i+2}}{\Delta\xi^2}, \quad 3 \le i \le N-2. \end{aligned} \tag{16}$$

This system of tridiagonal equations needs to be closed at boundaries, a diagonally dominant third-order compact scheme next to boundary points are used

$$\psi''_i - \psi''_{i+1} = \frac{\psi_{i-1} - 3\psi_i + 3\psi_{i+1} - \psi_{i+2}}{\Delta\xi^2}, \quad i = 2, \tag{17a}$$

$$\psi''_i - \psi''_{i-1} = \frac{\psi_{i+1} - 3\psi_i + 3\psi_{i-1} - \psi_{i-2}}{\Delta\xi^2}, \quad i = N-1. \tag{17b}$$

3. Solution of algebraic systems

The solution algorithm of the artificial compressibility formulation can be borrowed from those used for compressible flow computation. In this paper, the approximate factorization based alternate direction implicit scheme (AF-ADI) is used [2]. The details of the solution algorithm and its implementation can be found in [19]. The scheme is given as follows:

$$\begin{aligned} &\left[\mathbf{I} + \Delta\tau J\left(\bigtriangledown_\xi \hat{\mathbf{A}_\xi}^{+} + \bigtriangleup_\xi \hat{\mathbf{A}}^{-}_{\xi} - \delta_\xi\gamma_\xi\mathbf{I}_m\delta_\xi\right)\right] \\ &\times\left[\mathbf{I} + \Delta\tau J\left(\bigtriangledown_\eta \hat{\mathbf{A}_\eta}^{+} + \bigtriangleup_\eta \hat{\mathbf{A}_\eta}^{-} - \delta_\eta\gamma_\eta\mathbf{I}_m\delta_\eta\right)\right]\Delta\mathbf{D}^m = -\mathbf{R}^m, \end{aligned} \tag{18}$$

where $\delta^{\pm}_{\xi}\phi_i = \frac{\pm(\phi_{i\pm1} - \phi_i)}{\Delta\xi}$, $\delta_\xi\gamma_k\delta_\xi\phi_i = \frac{\gamma_{k_{i+1/2}}(\phi_{i+1} - \phi_i) - \gamma_{k_{i-1/2}}(\phi_i - \phi_{i-1})}{\Delta\xi^2}$.

To obtain the solution, we need to solve a block-tridiagonal equations in each directions. To simplify further, the split Jacobian matrices of the flux vectors in the LHS of above equation are approximately constructed by

$$\hat{\mathbf{A}}^{\pm} = \frac{1}{2}\left[\hat{\mathbf{A}} \pm \rho(\hat{\mathbf{A}})\mathbf{I}\right], \tag{19}$$

where

$$\rho(\hat{\mathbf{A}}) = \kappa \max\left[\left|\lambda(\hat{\mathbf{A}})\right|\right],$$

where $\lambda(\hat{\mathbf{A}})$ represents the eigenvalues of the matrix $\hat{\mathbf{A}}$, and κ is a constant that is greater than or equal to unity and we have used $\kappa \approx 1.2$ to get the stable solution [18].

4. Accuracy and convergence test: Kovasznay flow

The Kovasznay flow incorporates nonlinear effects and is therefore a good test for the accuracy of incompressible Navier-Stokes solvers [6, 12, 20]. In the domain $[-0.5 \times 0.5] \times [-0.5 \times 0.5]$, the analytical solution has the form:

$$u = 1 - e^{\lambda x}\cos 2\pi y,$$

$$v = \frac{\lambda}{2\pi} e^{\lambda x} \sin 2\pi y,$$
$$p = \frac{1}{2}(1 - e^{2\lambda x}),$$

where $\lambda = \frac{\mathrm{Re}}{2} - \sqrt{\left(\frac{\mathrm{Re}^2}{4} + 4\pi^2\right)}$. Dirichlet boundary conditions are specified using the exact solution. The stretching grids in the x-direction are generated using the transformation $\xi = \ln(x+1)$, $\eta = y$ with *inverse transformation* of the form $x = e^{\xi} - 1$, $y = \eta$. The iterations are continued until the residual drop to 10^{-12} as shown in Figures 2(a), (b). The stretching grids and streamlines contours for the steady solution corresponding to Re = 40 are shown in Figures 1(a) and (b) respectively.

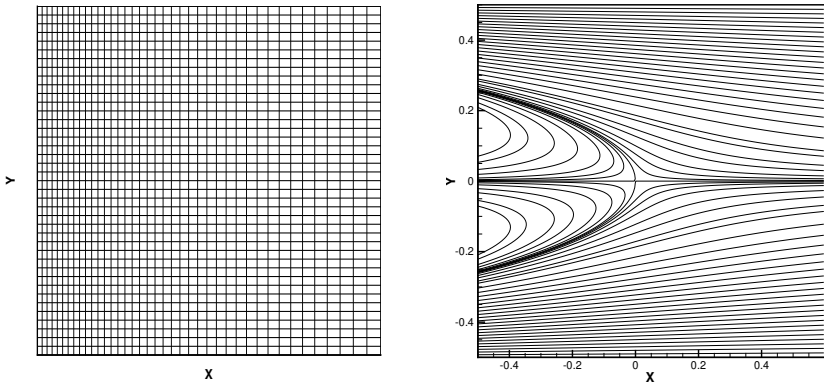

FIGURE 1. (a) Stretching grids, (b) Streamlines contours for the steady solution corresponding to Re = 40.

Table 1 shows the grid refinement study and accuracy analysis of the proposed scheme for Re = 40 and Re = 100. The high-order accuracy (nearly 5.0) is confirmed for the both velocity components and the pressure. The possible reason for not exactly 5.0 is the use of low-order schemes at the boundary. The order of accuracy O_A is calculated using the formula

$$O_A = \frac{\ln(e_2/e_1)}{\ln 2.0}$$

with

$$e_1 = \|\phi_e - \phi_f\|_2, \quad e_2 = \|\phi_e - \phi_c\|_2,$$

where ϕ_e, ϕ_f and ϕ_c stands for the exact solution, the solution on a fine grid and the solution on a coarser grid with half of the points in all directions respectively.

Figure 2(a) shows convergence history of the scheme at Re = 40 for different value of $\beta = 1, 10, 100, 500$. It can be seen that optimal convergence can be

TABLE 1. Errors and orders of accuracy using the proposed scheme for the Kovasznay flow.

Re = 40	u-velocity		v-velocity		pressure	
Mesh size	**L_2 error**	**Order u**	**L_2 error**	**Order v**	**L_2 error**	**Order p**
21×21	5.53×10^{-5}	–	1.89×10^{-5}	–	3.43×10^{-4}	–
41×41	2.52×10^{-6}	4.46	6.95×10^{-7}	4.77	1.30×10^{-5}	4.72
81×81	9.85×10^{-8}	4.68	1.81×10^{-8}	5.26	4.77×10^{-7}	4.77
161×161	4.21×10^{-9}	4.55	7.14×10^{-10}	4.66	1.94×10^{-8}	4.62
321×321	1.05×10^{-10}	4.76	2.34×10^{-11}	4.93	6.86×10^{-10}	4.82
Re = 100	**-**		**-**		**-**	
21×21	3.70×10^{-5}	–	7.18×10^{-6}	–	1.06×10^{-4}	–
41×41	1.83×10^{-6}	4.34	3.24×10^{-7}	4.47	3.97×10^{-6}	4.74
81×81	7.74×10^{-8}	4.56	8.25×10^{-9}	5.30	1.43×10^{-7}	4.80
161×161	3.40×10^{-9}	4.51	2.24×10^{-10}	5.20	5.27×10^{-9}	4.76
321×321	1.40×10^{-10}	4.60	6.76×10^{-12}	5.05	2.12×10^{-10}	4.64

achieved with $\beta = 10$ having error less the 10^{-12}. The nice thing about this solution is its existence for any Reynolds number as shown in Figure 2(b).

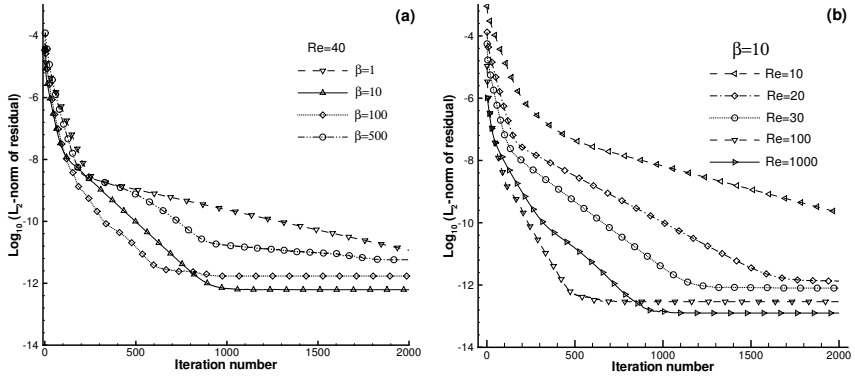

FIGURE 2. Convergence history (a) at fixed Re = 40 with different values of β and (b) at fixed $\beta = 10$ with different value of Re.

5. Numerical results

In this section, three benchmark problems like (i) 2D lid driven cavity flow with geometrical variations, (ii) flow in a channel with sinusoidal walls, and (iii) flow around an airfoil are solved numerically. Computations have been done on a sequential HP ProBook with processor Intel Core Duo at frequency 2.10GHz.

5.1. 2D lid driven cavity flow

This subsection is based upon the flow inside a lid driven cavity with variation of angles and boundary conditions. First problem is the classical lid driven cavity, the second problem is given with change of angles, and third and fourth problem is formulated with the change of boundary conditions. Comparison with reference results is provided for validation of the scheme.

5.1.1. *Classical lid driven cavity flow.* In this problem, the flow is given by moving the top boundary while no slip boundary conditions are applied on other solid walls. On the top wall ($y = 1.0$), boundary conditions are $u = u(x)$, $v = 0$ and p is computed from the y momentum equation $p_y = \frac{1}{\mathrm{Re}} v_{yy}$ imposed at the upper wall. Zero initial conditions are used for all variables. To avoid singularity at the top corners, the following hyperbolic tangent u-velocity on the top wall is used:

$$u\,(x) = \begin{cases} \tanh\,(100x)\,, & 0 \le x \le 0.5, \\ -\tanh\,(100(x-1))\,, & 0.5 < x \le 1. \end{cases}$$

We use 81×81 non-uniform grid which is clustered towards the walls using the stretching function $x_i = \frac{i}{i_{\max}} - \frac{\theta}{2\pi} \sin[\frac{2\pi i}{i_{\max}}]$, $0 < \theta \le 1$ in both x- and y-directions [11]. In Fig. 3(a), the computational domain while in Fig. 3(b) the streamline contours are presented for the Reynolds number $\mathrm{Re} = 5000$. It clearly shows the ability of the method to predict all the three (primary, secondary and tertiary) vortices correctly.

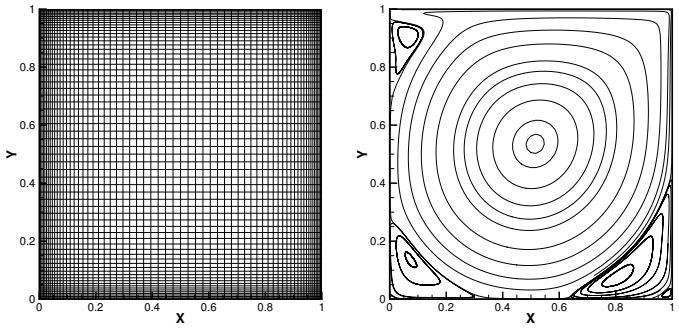

FIGURE 3. 2D lid driven cavity problem (a) Computational grid for $\theta = 0.6$ (b) Computed streamlines corresponding to $\mathrm{Re} = 5000$.

The comparisons of computed velocity components with the benchmark solution [9] for the $\mathrm{Re} = 100$ and $\mathrm{Re} = 5000$ are given in Figure 4. We can see that both the results match very well.

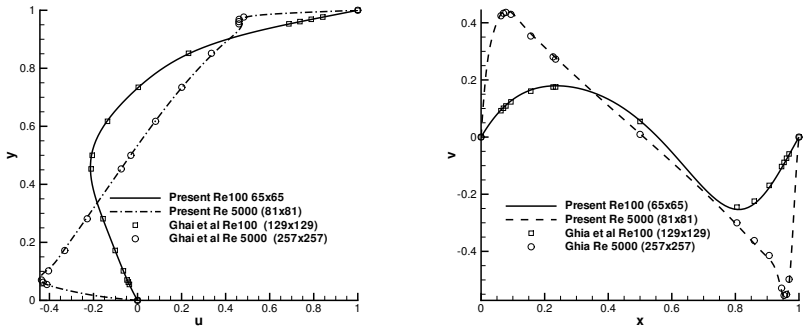

FIGURE 4. u and v-velocity components of velocity for Re = 100 and Re = 5000 compared with that of Ghia et al. [9].

5.1.2. *Flow inside skewed cavity.* Next, the flow inside a skewed cavity with the skew angle between $15^\circ < \alpha < 165^\circ$ with an increment of 15° is simulated. The grids are generated in such a way that the physical domain is mapped with the unit computational domain using the following transformation [15];

$$\xi = x - y\cot\alpha, \tag{20}$$

$$\eta = y\sin\alpha. \tag{21}$$

This transformation maps the non-uniform skewed cavity with the skew angle α to a uniform computational plane (ξ, η), that is directly dependant on skew angle α. The variation of α enforces us to modify the values of (ξ, η) as the computational plane is always equal to unit square. Since the mapping is one-one so the inverse transformation is given by:

$$x = \xi + \eta\cos\alpha, \tag{22}$$

$$y = \eta\sin\alpha. \tag{23}$$

The computed results are compared with the results given in [5] and are shown in Figure 5(a-b) for skew angle 30° and Figure 6(a-b) for skew angle 45°. A good agreement is observed with the reference solution. Furthermore, the comparison of results using angles 60°, 75°, 105° and 150° respectively are illustrated in Figure 7(a-b) and Figure 8(a-b) for Reynolds number 1000.

5.1.3. *Flow in two sided cavity.* In this subsection, the square cavity is driven such that the top and bottom walls are moving in parallel and in anti-parallel directions with fixed velocities. The streamlines pattern for parallel and anti parallel walls are respectively shown in Figure 9(a) and Figure 9(b). It is observed that parallel wall motion produces two vertices whereas the anti-parallel walls motion produces only one vertex.

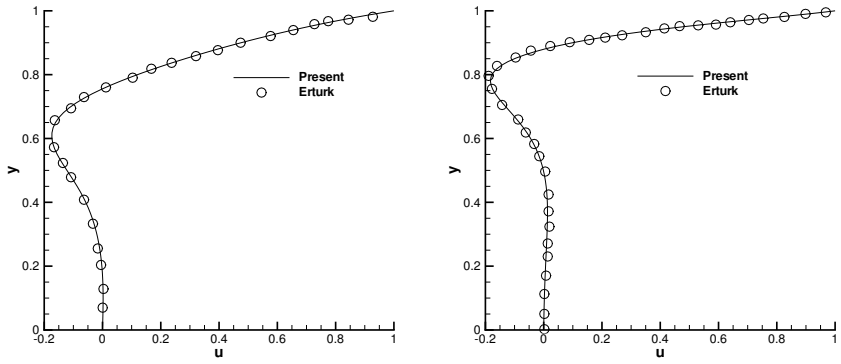

FIGURE 5. Comparison of normalized velocity u along y with Ref. [5] for skew angle $\alpha = 30°$ using grids size 101×101 (a) $\mathrm{Re} = 100$ (b) $\mathrm{Re} = 1000$.

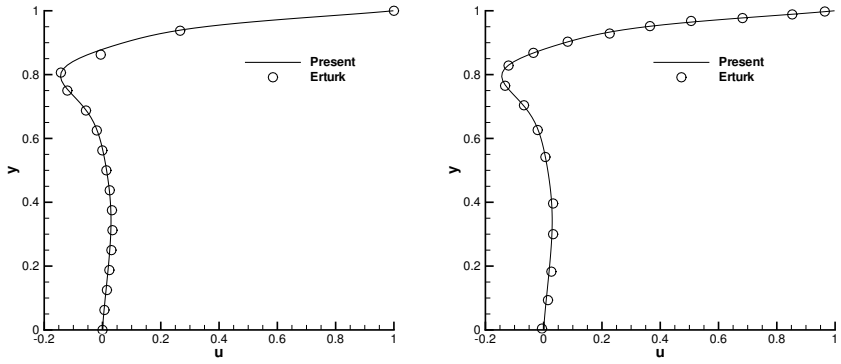

FIGURE 6. Comparison of normalized velocity u along y with Ref. [5] for skew angle $45°$ (a) $\mathrm{Re} = 100$ (b) $\mathrm{Re} = 1000$.

The normalized velocity $u = u(y)$ in square cavity along parallel and anti-parallel directions are compared with Ref. [16] results and a good agreement is observed which is shown in Figure 10(a-b).

5.1.4. *Flow in a four sided cavity.* Finally, the flow inside a cavity with four sides moving with following velocities

$u = 0,\ v = 1$ at left boundary, $u = 0,\ v = -1$ at right boundary and

$u = 1,\ v = 0$ at top boundary, $u = -1,\ v = 0$ at bottom boundary.

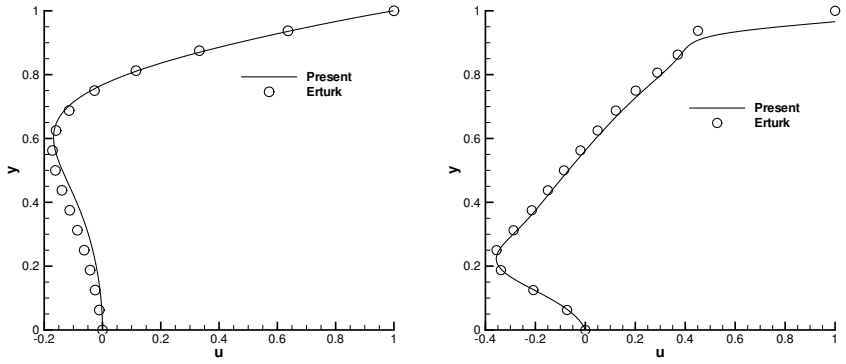

FIGURE 7. Comparison of normalized velocity u along y with Ref. [5] using Re = 1000 for skew angles (a) $\alpha = 60°$ (b) $\alpha = 75°$.

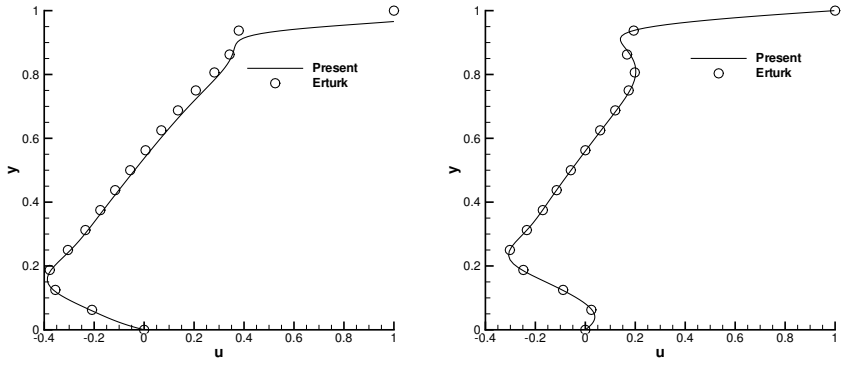

FIGURE 8. Comparison of normalized velocity u along y with Ref. [5] using Re = 1000 for skew angles (a) $\alpha = 105°$ (b) $\alpha = 150°$.

is studied. The streamlines pattern is illustrated in Figure 11(a) for grids 101×101 while comparison of u velocity versus y with the reference solution [1] is given in Figure 11(b) with Reynolds number 100. We see that the comparison agree well.

5.2. Flow in a sinusoidal channel

The second problem for testing the efficiency of the scheme is the flow in a symmetric channel with sinusoidal walls as shown in Figure 12.

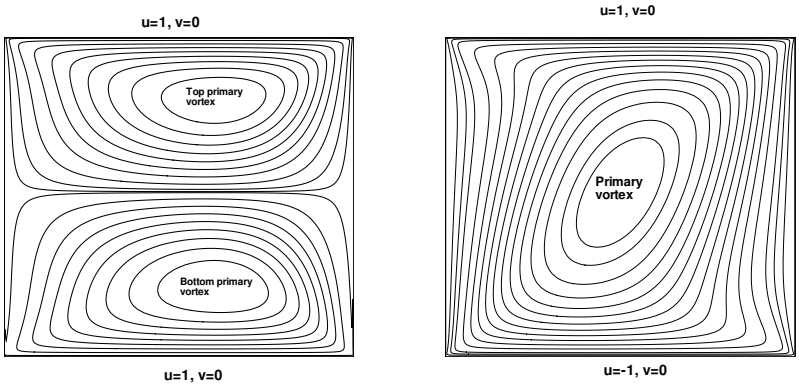

FIGURE 9. Streamline pattern for the two sided cavity flow (a) Parallel wall motion (b) Antiparallel wall motion.

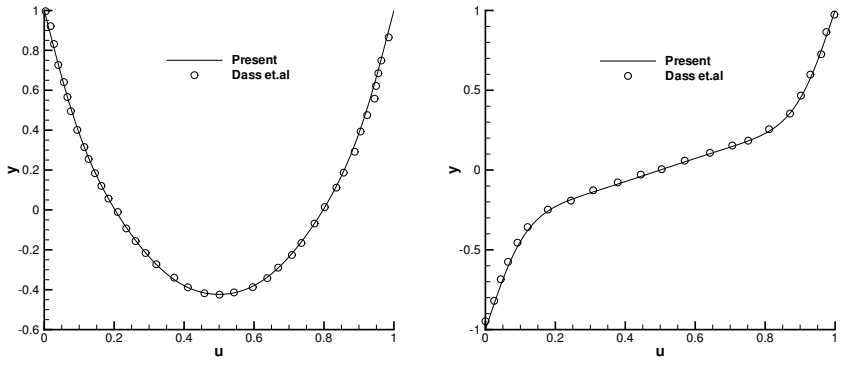

FIGURE 10. Comparison of normalized velocity u vs y for two sided lid driven cavity flow at Re = 100 compared with Ref. [16]. (a) parallel (b) anti-parallel.

The grid are generated using the transformation $x = \xi$ and $y = \eta(1 - \varepsilon\cos\xi)$ with ε as wall amplitude. At the inlet $u = \frac{3}{2}(1 - y^2)$ and $v = 0$ while p is extrapolated using the interior mesh points. At the outlet boundary $\frac{\partial u}{\partial x} = 0$ and $\frac{\partial v}{\partial x} = 0$ while pressure is taken to be zero. On the upper stationary wall, no slip boundary condition is applied for velocity and zero normal pressure is applied whereas $u_y = 0,\ p_y = 0$ and $v = 0$ are used at the central line. The formation of vortices depends mainly upon the viscosity and hence on Reynolds number Re and on perturbation parameter ε. We simulated the problem for

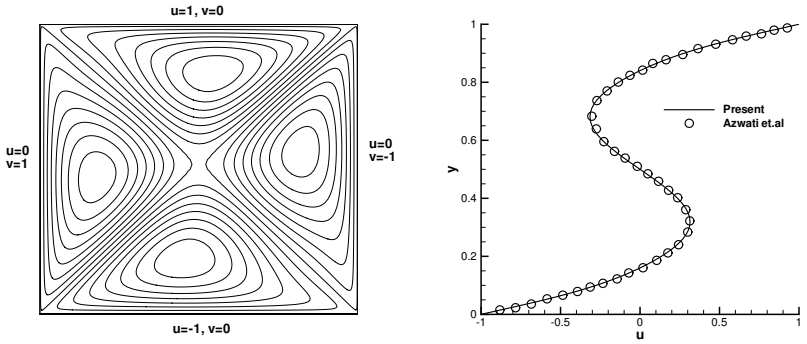

FIGURE 11. Flow inside four sided cavity at Re = 100. (a) Streamlines for four sided cavity (b) Plot of normalized u versus y compared with Ref. [1].

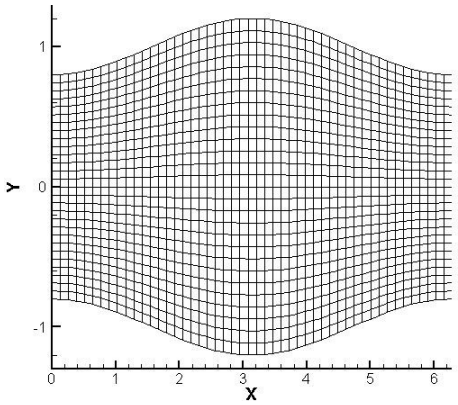

FIGURE 12. Geometry of the channel

different Re and different ε but presented only the case with $\varepsilon = 0.2$ and Re = 400 for comparison purpose with the numerical result [14]. We see that the qualitative comparison is very good as shown in Figure 13.

5.3. Viscous flow around an airfoil

In this problem we simulate the viscous flow over a NACA-0012 airfoil of unit chord length c at 0° angle of attack. The computational plane is O-type nonuniform grids clustered near the airfoil. The computational domain is big enough $[-10, 10]$, so that the outer boundary is governed by freestream conditions. A unit inflow velocity is used on the lateral and circular boundaries of

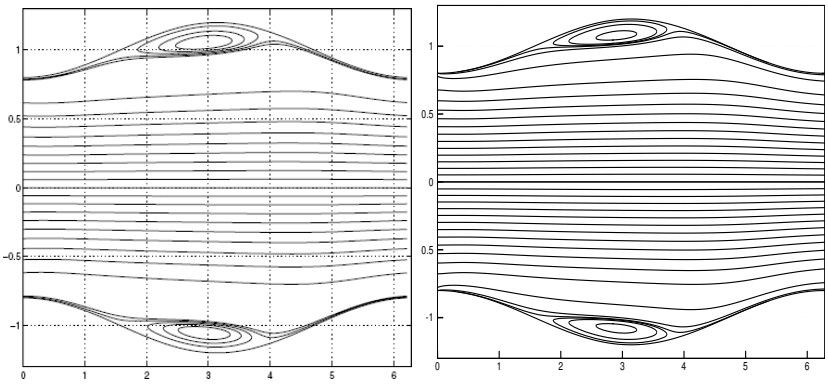

FIGURE 13. Comparison of the stream lines [LHS [14] and RHS present] with $\varepsilon = 0.2$ and $\mathrm{Re} = 400$ presenting the separation regions for the flow field.

airfoil. The periodic boundary conditions are specified in the span-wise direction. It is useful to cluster of the grid lines near the airfoil surface and in the wake downstream, where the flow-properties (like velocity) have high gradients. Clustering of gridlines in these areas allow to tackle the high gradients without having to highly resolve the whole domain as shown in the Figure 14(a) and Figure 14(b). We have used 129×65 O-type grid given in Figure 14(b) for the present calculations. Very slow convergence is observed for the grids given in Figure 14(a).

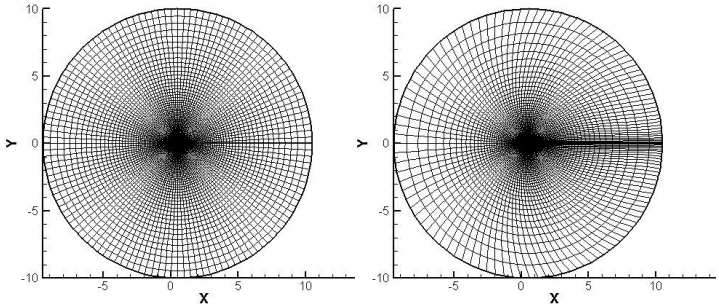

FIGURE 14. Computational grid around an airfoil (a) unclustered in the wake downstream (b) clustered in the wake downstream.

Figure 15(a) shows a close view of the grid so that we can see the airfoil geometry clearly. To compare with available data, we solve the problem for $\mathrm{Re} = 2.8 \times 10^6$ and different values of β. Pressure contours around the airfoil is shown Figure 15(b).

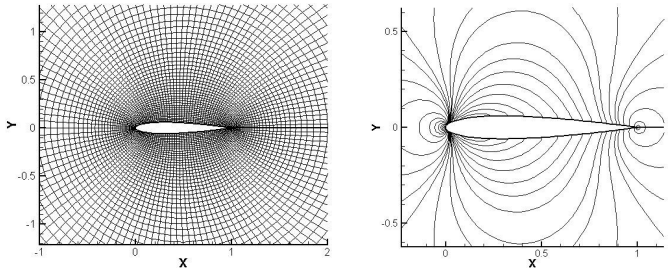

FIGURE 15. Flow past an airfoil (a) closed view of grid 14(b) and (b) computed pressure contours.

In Figure 16, the computed surface pressure distribution for grids 14(a) and 14(b) are compared with the reference approximate digitized data of Gregory and Reilly [10]. A good agreement is observed for grids 14(b), however, there is some deviation for grids 14(a). This test problem shows the proposed model is accurate and flexible and the formulation is also applicable to complex flows.

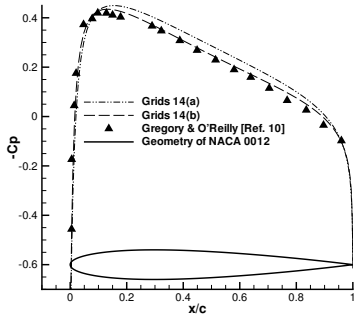

FIGURE 16. Comparison of surface pressure coefficients at $\mathrm{Re} = 2.88 \times 10^6$.

6. Conclusions

A high-order upwind compact finite difference scheme in the generalized coordinate system is developed for the solution of 2D incompressible Navier-Stokes equations using artificial compressibility method. Both Dirichlet and Neumann boundary conditions are easily incorporated into the numerical scheme. Convergence and high-order of accuracy are verified using a test problem having an exact solution. To bring out the advantage of the scheme, we use it for computing several benchmark problems on non-uniform grids. The results obtained for these test cases on relatively coarser grids are compared

with existing numerical results. The scheme is high-order accurate and capable of handling problems with complex geometries using non-uniform grids.

References

[1] C. Azwadi, A. Rajab, and S. Sofianuddin, *Four sided lid-driven cavity flow using time splitting method of Adam Bashforth scheme*, Int. J. of Autom and Mech. Eng. (IJAME) **9** (2014), 1501–1510.

[2] R. Beam and R. F. Warming, *An implicit scheme for the compressible Navier-Stokes equations*, AIAA J. **16** (1978), 393–402.

[3] A. J. Chorin, *A numerical method for solving incompressible viscous flow problems*, J. Comput. Phys. **2** (1967), 12–26.

[4] J. A. Ekaterinaris, *High-order accurate numerical solutions of incompressible flows with the artificial compressibility method*, Internat. J. Numer. Methods Fluids **45** (2004), no. 11, 1187–1207.

[5] E. Erturk and B. Dursun, *Numerical solution of 2D steady incompressible flow in a driven skewed cavity flow at high Reynolds numbers*, Z. Angew Math. Mech. **87** (2007), no. 5, 377–392.

[6] H. Fadel, M. Agouzoul, and P. K. Jimack, *High-order finite difference schemes for incompressible flows*, Internat. J. Numer. Methods Fluids **65** (2011), no. 9, 1050–1070.

[7] D. Fu and Y. Ma, *A high order accurate difference scheme for complex flow fields*, J. Comput. Phys. **134** (1997), no. 1, 1–15.

[8] D. Fu, Y. Ma, and T. Kobayashi, *Nonphysical oscillations in numerical solutions*: *reason and improvement*, CFD J. **4** (1996), no. 4, 427–450.

[9] U. Ghia, K. N. Ghia, and C. T. Shin, *High Re solutions for incompressible Navier-Stokes equations*, J. Comput. Phys. **49** (1983), 387–411.

[10] N. Gregory and C. L. O'Reilly, *Low speed aerodynamic characteristics of NACA 0012 airfoil section, including the effects of upper surface roughness simulation hoarfrost*, Aero Report 1308, National Physics Laboratory, Teddington, U.K., 1970.

[11] J. C. Kalita, A. K. Dass, and N. Nidhi, *An efficient transient Navier-Stokes solver on compact nonuniform space grids*, J. Comput. Appl. Math. **214** (2008), no. 1, 148–162.

[12] L. I. G. Kovasznay, *Laminar flow behind two-dimensional grid*, Proc. Cambridge Philos. Soc. **44** (1948), 58–62.

[13] S. K. Lele, *Compact finite difference schemes with spectral-like resolution*, J. Comput. Phys. **103** (1992), no. 1, 16–42.

[14] H. Luo and T. R. Bewley, *On the contravariant form of the Navier-Stokes equations in time-dependent curvilinear coordinate systems*, J. Comput. Phys. **199** (2004), no. 1, 355–375.

[15] R. Nayak, S. Batachariya, and I. Pop, *Numerical study of mixed convection and entropy generation of Cu-Water nano fluid in a differentially heated skewed enclosure*, Int. J. Heat and Mass Transfer **85** (2015), 620–634.

[16] A. D. Perumal and K. A. Dass, *Simulation of incompressible flows in two-sided lid-driven square cavities. Part II - LBM*, CFD Letters **2**(2010), no. 1, 25–38.

[17] P. L. Roe, *Approximate Riemann solvers, parameter vectors, and difference schemes*, J. Comput. Phys. **43** (1981), no. 2, 357–372.

[18] S. E. Rogers and D. Kwak, *An upwind differencing scheme for the incompressible Navier-Stokes equations*, Appl. Numer. Math. **8** (1991), no. 1, 43–64.

[19] A. Shah, H. Guo, and L. Yuan, *A third-order upwind compact scheme on curvilinear meshes for the incompressible Navier-Stokes equations*, Commun. Comput. Phys. **5** (2009), no. 2-4, 712–729.

[20] A. Shah, L. Yuan, and A. Khan, *Upwind compact finite difference scheme for time-accurate solution of the incompressible Navier-Stokes equations*, Appl. Math. Comput. **215** (2010), no. 9, 3201–3213.
[21] M. R. Visbal and D. V. Gaitonde, *On the use of higher-order finite-difference schemes on curvilinear and deforming meshes*, J. Comput. Phys. **181** (2002), no. 1, 155–185.

Hassan Fayyaz
Department of Mathematics
COMSATS Institute of Information Technology
Park Road, Islamabad 45550, Pakistan
Email address: hfkiani@gmail.com

Abdullah Shah
Department of Mathematics
COMSATS Institute of Information Technology
Park Road, Islamabad 45550, Pakistan
Email address: abdullah_shah@comsats.edu.pk